This paper first appeared in the thirteenth print edition of the *Photovoltaics International* journal, published in August 2011.

Polarized light metrology for thin-film photovoltaics: Manufacturing-scale processes

Robert W. Collins, **Lila R. Dahal** & **Nikolas J. Podraza**, Center for Photovoltaics Innovation & Commercialization and Department of Physics & Astronomy, University of Toledo, Toledo, Ohio, **Kenneth R. Kormanyos**, Calyxo USA, Perrysburg, Ohio, & **Sylvain Marsillac**, Department of Electrical & Computer Engineering, Old Dominion University, Norfolk, Virginia, USA

ABSTRACT

In situ, real-time and off-line polarization spectroscopies have been applied in studies of large-area spatial uniformity of the components of multilayer stacks in hydrogenated silicon (Si:H) and cadmium telluride (CdTe) thin-film photovoltaic (PV) technologies. Such reflection spectroscopies involve first the measurement of spectra in the reflected-to-incident polarization state ratio of the light wave (or the ellipsometry angles of the reflecting multilayer stack), and then the analysis of these spectra to determine the thicknesses and properties of component layers of the stack. In addition, expanded capabilities result from measurement/analysis of the irradiance ratio and the degree of polarization of the reflected beam, simultaneously with the polarization state ratio, particularly for rough surfaces with in-plane roughness scales of the order of the optical wavelength or greater that scatter and depolarize the light beam. This paper provides examples of 1) real-time monitoring of texture etching of the transparent conducting oxide ZnO:Al; 2) real-time monitoring and off-line mapping of roll-to-roll deposited hydrogenated amorphous silicon (a-Si:H); and 3) large-area mapping of coated glass panels used in low-cost CdTe PV technology. For a-Si:H and CdTe thin-film PV technologies, the focus is on the characterization of the window layers, which are *p*-type protocrystalline Si:H and *n*-type cadmium sulphide (CdS), respectively. Analysis of the thickness, phase and structure of the window layer material over the area of the PV panel is critical in order to design processes for uniformity of high performance. Descriptions are given of future directions in novel instrumentation development that will enable mapping for uniformity evaluation at the high speeds required for on-line analysis.

Introduction

Non-invasive monitoring and control tools are needed on production lines for thin-film photovoltaic module manufacturing [1]. Polarized light spectroscopy is valuable in this application due to its capacity for rapid measurement of film thicknesses in multilayer stacks – even at the sub-nanometre level of sensitivity – by exploiting the experimental techniques of multichannel spectroscopic ellipsometry (SE) at a single sample spot [2]. Additional film properties, such as the composition or crystalline grain size, influence the wavelength dependence of the index of refraction and extinction coefficient (n, k) (alternatively expressed as the complex dielectric function ($\varepsilon = \varepsilon_1 + i\varepsilon_2$)) of the films, and, as a result, can be extracted in the same optical analysis that provides thicknesses [3]. It is advantageous to use *ellipsometry* over *reflectometry* because the former involves measurement of two parameters related to a ratio of the polarization properties of a light wave after and before oblique reflection. In contrast, reflectometry involves measurement of one parameter – the ratio of the irradiance property.

The information content in the polarization state of a light wave at a given wavelength is derived from the AC characteristics of an oscillatory irradiance waveform at the associated pixel of the ellipsometer's multichannel detection system [2]. These characteristics include the AC component phases and their amplitudes relative to the DC component. In contrast, the irradiance is derived from the DC component alone. As a result, small fluctuations in the position of the detected light beam due to photovoltaic (PV) substrate/film motion during continuous on-line measurement affect optical alignment and thus calibration of the irradiance measurement. In contrast, the polarization state measurement is self-calibrating with respect to irradiance, through continuous normalization of the AC component by the DC component. Furthermore, because of the determination of a phase difference shift upon reflection, the polarization measurement is much more sensitive to the very thin layers of the PV stack than the irradiance measurement. In spite of the challenges of maintaining irradiance calibration, it is valuable to perform irradiance, polarization state, and degree of polarization measurement and analysis simultaneously, as in *polarimetry*. This approach is particularly well suited for measurements of rough surfaces, in which case the predicted reflected irradiance from a polarization analysis can be compared with the measured reflected irradiance to extract information about haze – light loss from the specular beam due to scattering by the substrate/film [4].

With the integration of a multichannel detection system for high-speed ellipsometric spectroscopy and with the expansion of the spectral range, SE has gained significant analytical power for on-line monitoring of thin-film fabrication [2,4–7]. As a consequence, minimum acquisition times for full spectra of the order of tens of milliseconds are possible. These spectra yield thickness and optical property information about a wide variety of materials from metallic and transparent conducting oxide contacts to dielectric antireflecting and semiconducting materials, the latter with bandgaps over the solar photon energy range of 0.8 to 2.5eV [3]. The analysis of data collected in on-line and off-line applications poses a significant challenge, and the development of multilayer optical models along with (n, k) databases in the research laboratory reduces the analysis of a complex multilayer stack to the determination of a set of wavelength-independent parameters. These parameters include not only thickness but also basic material properties of composition, crystalline grain size, stress and temperature – properties that define (n, k) [3,8].

Examples to be presented in this paper of metrology applications based on multichannel ellipsometry as a polarization spectroscopy include previous and ongoing activities in texture etching of aluminium-doped zinc oxide (ZnO:Al), an application that demonstrates the full potential of a polarimetric analysis [4]; on-line, single-spot analysis of thin-film

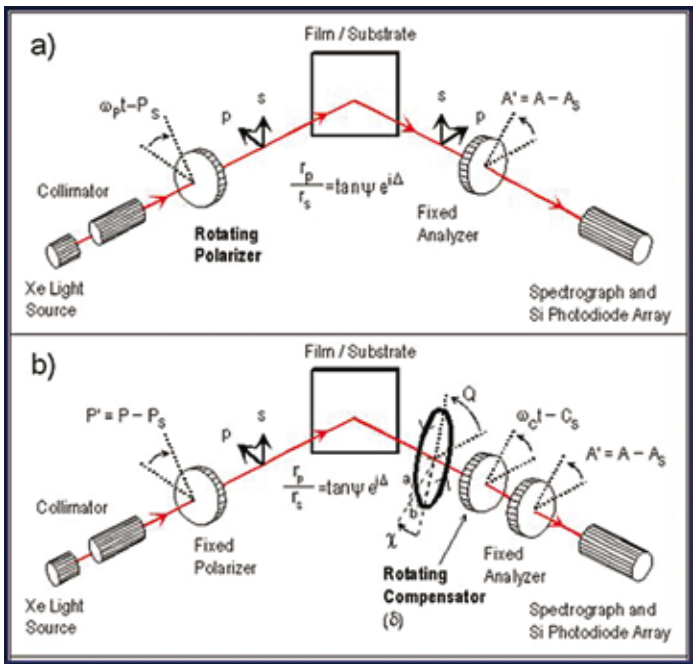

Figure 1. Two multichannel designs for high-speed measurements: (a) rotating polarizer configuration for ellipsometry, and (b) rotating compensator configuration for polarimetry. Both instruments enable measurement of spectra in the ellipsometry angles (ψ, Δ); for an isotropic sample, these angles are related to the *p*-to-*s* ratio of complex amplitude reflection coefficients according to $\tan\psi \exp(i\Delta) = r_p/r_s$. The rotating compensator instrument shown in (b) also has polarimetric capability through measurement of the reflected beam Stokes vector, which incorporates the irradiance I_r, the tilt angle Q_r and ellipticity angle χ_r of the ellipse of polarization, and the degree of polarization p_r.

hydrogenated silicon (Si:H) solar cells in roll-to-roll fabrication [9]; off-line, large-area, multispot mapping of multilayer stacks used in cadmium telluride (CdTe) technology [10]; and future directions in expanded-beam imaging analysis for mapping of rigid and flexible roll-to-roll substrates undergoing linear motion on the production line [11]. Given existing bright sources and high-speed two-dimensional array detectors, the last application of imaging/mapping spectroscopy shows promise for monitoring large-area coated substrates at the linear substrate/film speeds used in production.

Multichannel spectroscopic ellipsometry and polarimetry

Instrumentation

Fig. 1 shows schematics of ellipsometric and polarimetric instruments that have been developed to probe substrate/film structures with a single beam spot, ranging in size from ~0.1 to 10mm [2]. As depicted in Figs. 1(a) and (b), respectively, these instruments use a continuously rotating polarizer or retarder (also called a 'compensator') to measure the effect of the sample on the incident beam polarization state. The light source – such as Xe, D_2 and tungsten halogen lamps, individually or in tandem – is designed for broadband emission. The detection system consists of a spectrograph and one or more linear detector arrays, also designed for broadband detection, with the widest spectral range spanning from 0.19 to 1.7μm [5–7]. Because typical mechanical rotation frequencies ω/2π of the polarizer or compensator range from 5 to 50Hz, a single ellipsometry or polarimetry measurement can be performed in a time of π/ω (half mechanical cycle), ranging from 10 to 100ms. In this time, the array detector(s) must be scanned a minimum of three times for the rotating polarizer instrument in Fig. 1(a) to extract ellipsometric spectra, and five times for the rotating compensator instrument in Fig. 1(b) to extract polarimetric spectra. In many applications, a 10–100ms acquisition time is not needed, and so the spectra are collected as averages over ~100 measurement cycles to improve signal-to-noise ratio, leading to an acquisition time of 1 to 10 seconds.

For both instruments, the typical data output consists of (ψ, Δ) spectra, which can be extracted in a single cycle in a time as short as ~10ms, or from an average of cycles in ~1 second [2]. The (ψ, Δ) values can be understood by an analogy with the reflectance as follows. For a polarized optical plane wave obliquely incident on a surface, one can identify both an irradiance I_i (describing the energy crossing a unit area per unit time) and a polarization state $\xi_i = (E_{xi}/E_{yi}) \exp[i(\delta_{xi} - \delta_{yi})]$ (describing the relative amplitudes E_{xi}/E_{yi} and the phase difference $\delta_{xi} - \delta_{yi}$ for two orthogonal *x*-*y* field components). The reflectance of a surface is defined as the ratio of the irradiance in the reflected beam to that in the incident beam: $R = I_r/I_i$. Reflectometry involves measuring R as a function of wavelength. Similarly, the ellipsometry angles are defined by the ratio of the reflected beam polarization state to the incident beam polarization state: $\tan\psi\exp(i\Delta) = \xi_r/\xi_i$. Thus, $\tan\psi$ is a ratio (reflected-to-incident) of relative amplitudes and Δ is a shift (upon reflection) in the phase difference. In this case, the *x* and *y* orthogonal axes are the *p* and *s* directions of the reflecting surface, parallel (*p*) and perpendicular (*s*) to the plane of incidence, which is defined as the plane that contains the incident and reflected propagation vectors of the plane waves. Combining the expressions for (ψ, Δ) and ξ, one can show that, for an isotropic sample, $\tan\psi \exp(i\Delta) = r_p/r_s$, where r_p and r_s are the complex amplitude reflection (or Fresnel) coefficients for linearly polarized light with electric fields vibrating along the *p* and *s* directions.

Although the rotating polarizer ellipsometer in Fig. 1(a) is the simplest such design, its simplicity leads to limitations [2]. If the substrate is non-absorbing and incorporates a very thin film on its surface, e.g. the first layer of a transparent conducting oxide stack on glass, then incident linearly polarized light is reflected as nearly linearly polarized light. Under these conditions, accuracy in the determination of the film properties is reduced. In addition, if the thin film is rough on the scale of geometric optics or is spatially non-uniform, depolarization of the incident beam will occur. This means that, over the cross-section of the light beam, a distribution of polarization states will be generated due to the distribution of local thicknesses or film properties. If unrecognized, this depolarization effect can be misinterpreted as an increase in ellipticity angle of the polarization state when the rotating polarizer ellipsometer is used; in fact, this ellipsometer configuration cannot distinguish randomly polarized or unpolarized light reflected by the sample from circularly polarized light. For these reasons, the more advanced version of the ellipsometer with a rotating compensator as shown in Fig. 1(b) is necessary to provide polarimetric data – independent measurements that can separate the polarization ellipse and the degree of polarization – and is preferable in studies of the very rough surfaces and interfaces that may be encountered in thin-film PV (even if the separate information about the degree of polarization is not exploited).

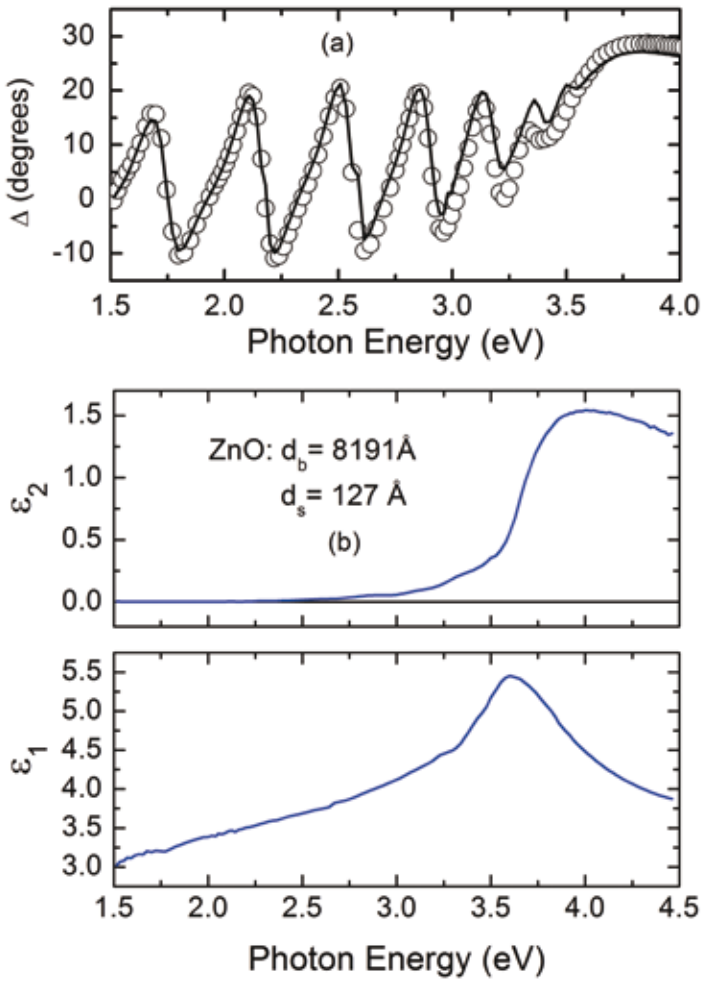

Figure 2. (a) Best fit (solid line) to the measured spectrum in the ellipsometry angle Δ (points) for a ZnO:Al film on glass, prior to etching with 22ppm (by vol.) HCl in H_2O for macroscopic roughness enhancement; (b) dielectric function of the ZnO:Al film along with its microscopic surface roughness and bulk layer thicknesses (d_s, d_b) deduced in the fit. The real and imaginary parts, ε_1 and ε_2, of the dielectric function ε are related to the index of refraction n and the extinction coefficient k via the expressions $\varepsilon_1 = n^2 - k^2$ and $\varepsilon_2 = 2nk$.

Operationally, the compensator acts on the polarization state in a similar way to a reflecting sample, but with three differences [12]: 1) it operates in transmission at normal incidence (rather than in reflection at oblique incidence); 2) the orthogonal coordinate system consists of fast (*F*) and slow (*S*) axes which are defined, not by the incident beam, but rather by the orientation of the compensator component crystal(s); and 3) the ratio of relative amplitudes (transmitted-to-incident) is unity for an ideal device, meaning that the polarization state ratio is given by $\exp(i\delta) = \xi_t/\xi_i$, where δ is the shift upon transmission in the *S-F* phase difference. Because of this phase-shifting ability of the compensator, it serves, in conjunction with the second fixed polarizer (or analyzer) in Fig. 1(b), as a polarimeter, meaning that when rotated it can extract all four components of the Stokes vector of the reflected light beam. The Stokes vector incorporates not only polarization information – the tilt angle Q_r and ellipticity angle χ_r of the reflected beam polarization state – but also the reflected irradiance I_r and the degree of polarization p_r. From this set of spectra, one can extract not only the standard ellipsometry angles of the sample (ψ, Δ), but also direct information on thin-film non-idealities associated with non-uniformities and geometric optics scale roughness, as will be described in the next part of this section.

Advanced data analysis for rough surfaces

In this illustrative example, a rotating compensator instrument has been used in a full polarimetric analysis of rough surfaces that are often encountered in thin-film PV manufacturing [4]. A glass substrate coated with ZnO:Al, which acts as a transparent conductor, has been 'texture etched' in a solution of ~22ppm HCl by volume in H_2O while monitoring with real-time SE. Texture etching involves enhancing the macroscopic roughness, which leads to greater light scattering by the film. This in turn promotes light trapping within the photoactive intrinsic (or *i*) layer when a thin-film Si:H solar cell in either the *p-i-n* or the *n-i-p* sequence is deposited on the surface of the substrate/ZnO:Al. Fig. 2(a) shows the starting Δ spectrum for the glass/ZnO:Al before etching and a best fit, which (along with corresponding results for ψ) provides the optical properties, bulk layer thickness d_b and microscopic roughness layer thickness d_s given in Fig. 2(b). The initial values at t = 0 of (d_b, d_s) before etching are (8191Å, 127Å); the final values after 30 minutes of etching are (7969Å, 232Å). The *microscopic roughness* deduced in this analysis is defined as roughness with an in-plane scale on the atomic level and above (1–500Å), but remaining much less than the central wavelength of the probe beam (~5000Å). This roughness is simulated using standard ellipsometry analysis, replacing the rough surface region with a discrete surface layer having well-defined interfaces to the ambient and underlying 'bulk' layer. The thickness of this surface layer describes the amplitude of the surface modulations, and the optical properties of the layer are described by the Bruggeman effective medium theory [13].

Two results can be expected from the polarimetric data in the absence of roughness on scales larger than the above-described microscopic scale. In the absence of *macroscopic* roughness (having an in-plane scale 500Å to 5μm – within an order of magnitude of the central wavelength of the probe beam), the measured reflectance is predictable from the ZnO:Al bulk layer thickness, its microscopic surface roughness layer thickness, and the glass substrate and ZnO:Al thin-film optical properties (n, k). In the absence of geometric optics scale roughness (having an in-plane scale 5μm to 5mm – much greater than the central probe wavelength, greater than the lateral coherence of the light beam, but smaller than the beam spot on the substrate/film) and in the absence of other non-uniformities (e.g. large-scale thickness gradients), the fraction of the irradiance that is not purely polarized ($1 - p_r$) is expected to be zero.

Even for the starting ZnO:Al-coated substrate, however, the reflectance measured experimentally deviates from that predicted by the ellipsometry model, as shown in the top panel of Fig. 3 (open circles). The difference – characterized by a lower measured reflectance spectrum than the prediction – can be understood in terms of light scattering by macroscopic roughness and can be modelled using a simple scalar light-scattering theory [14]. This theory yields reflection and transmission coefficients c_j ($c = r, t$; $j = p, s$) of the form

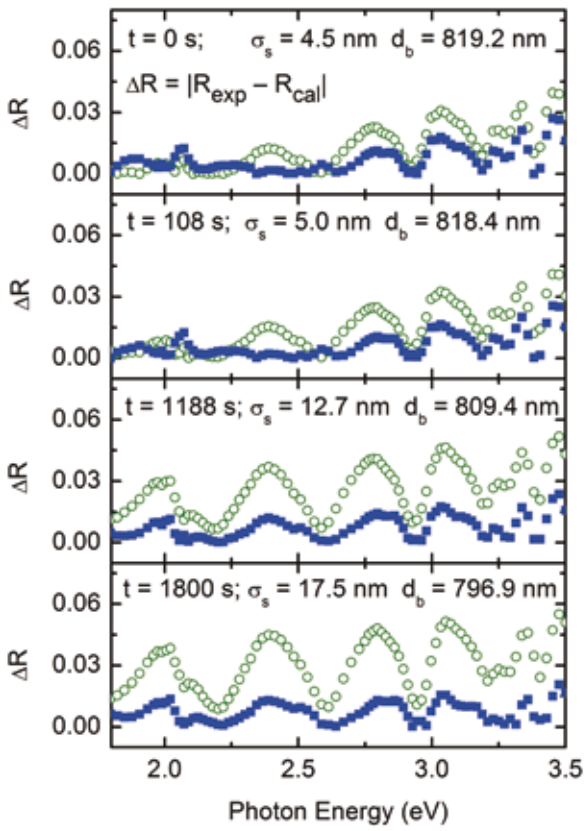

Figure 3. Difference between the experimental and predicted unpolarized specular reflectance spectra for the ZnO:Al sample at four different times during etching. The open points are the results of a prediction assuming an ideal specularly reflecting surface without macroscopic roughness ($\sigma_s = 0$); the filled squares are the results of a prediction on the basis of scalar diffraction theory, leading to best-fit macroscopic roughness thickness values σ_s as follows: 1) t = 0s, σ_s = 45Å; 2) t = 108s, σ_s = 50Å; 3) t = 1188s, σ_s = 127Å; and 4) t = 1800s, σ_s = 175Å.

$c_j = c_j(0)\ \exp(-\sigma_s \Delta k_z)$, where Δk_z is the change in z-component of the propagation vector upon reflection or transmission and σs is the width of the surface height distribution, which is assumed to be Lorentzian, $h(z) = (2\sigma_s/\pi)(4z^2 + \sigma_s^2)^{-1}$. The top panel of Fig. 3 shows a smaller difference between the experimental reflectance and the prediction when this theory is applied (filled squares). A best-fit value of σ_s = 45Å is found for the width of the Lorentzian distribution, which yields better fits in this study than the more commonly used Gaussian distribution [14]. In the scalar light-scattering theory, *p* and *s* polarizations are reduced by the same amplitude, and, although the reflectance is reduced, the polarization of the specularly reflected beam is unaffected. As etching proceeds, the deviation of the measured reflectance from the ellipsometric prediction increases, and this deviation enables the determination of the time evolution of σ_s, a measure of the macroscopic roughness thickness, as shown in the lower panels of Fig. 3. Using this simple scattering theory, residual deviations between the measured and predicted reflectance are of the order of the irradiance calibration uncertainties.

For the glass/ZnO:Al before etching, very weak features near 2.2, 2.6 and 2.9eV can be observed in the depolarization spectra of the reflected beam (see the topmost panel of Fig. 4; open circles). This in turn implies that the unetched film exhibits non-uniformity on in-plane scales larger than the lateral coherence length of the light wave (> 5μm); the non-uniformity is associated with geometric optics scale roughness, but near the instrument detection limits. As etching proceeds, these weak features in the depolarization spectra

are enhanced, as shown by the results in the lower two panels of Fig. 4. These spectra have been modelled assuming an incoherent superposition of irradiance waveforms from the probed area of the film and a Lorentzian film thickness distribution with an average thickness value deduced from the (ψ, Δ) spectra. The only free parameter in the analysis is the width of the distribution, which controls the height of the depolarization features. The width is determined to be 21Å at the onset of etching (which represents a 0.25% thickness variation over the beam area), and this value increases by more than a factor of three as etching proceeds (see bottom panel in Fig. 4).

Fig. 5 summarizes the results for the evolution of the microscopic, macroscopic and geometric optics scale roughness thicknesses during the etching process. The results are in reasonable agreement with ex situ atomic force microscopy (AFM) and profilometry on companion samples etched under the same conditions but for intermediate etching times. To evaluate microscopic and macroscopic roughness, the AFM rms roughness was measured from 0.2 × 0.2μm^2 and 10 × 10μm^2 images, respectively; and to evaluate geometric optics scale roughness, 5mm-long profilometry scans were analyzed. The lower value of roughness from profilometry is a consequence of its inability to detect roughness on the 5–50μm in-plane scale.

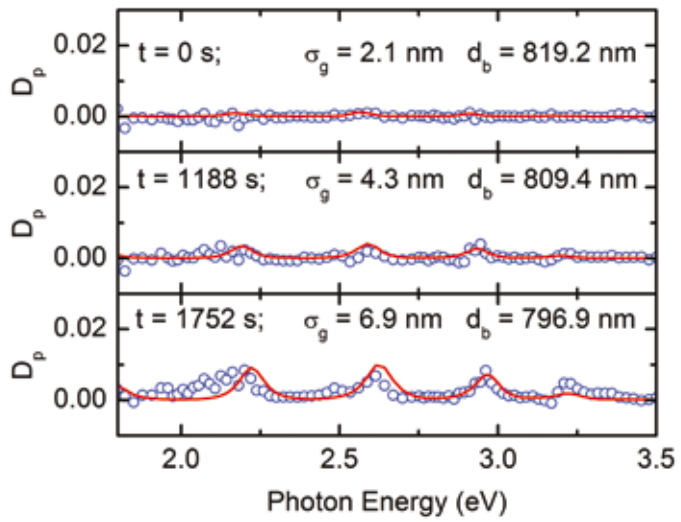

Figure 4. Experimental depolarization spectra for the ZnO:Al sample at three different times during etching (open points); also shown are modelled spectra based on incoherent superposition of irradiance waveforms from regions of different bulk layer thickness (solid lines), yielding geometric optics scale roughness thickness values σ_g as follows: 1) t = 0s, σ_g = 21Å; 2) t = 1188s, σ_g = 43Å; and 3) t = 1752s, σ_g = 69Å.

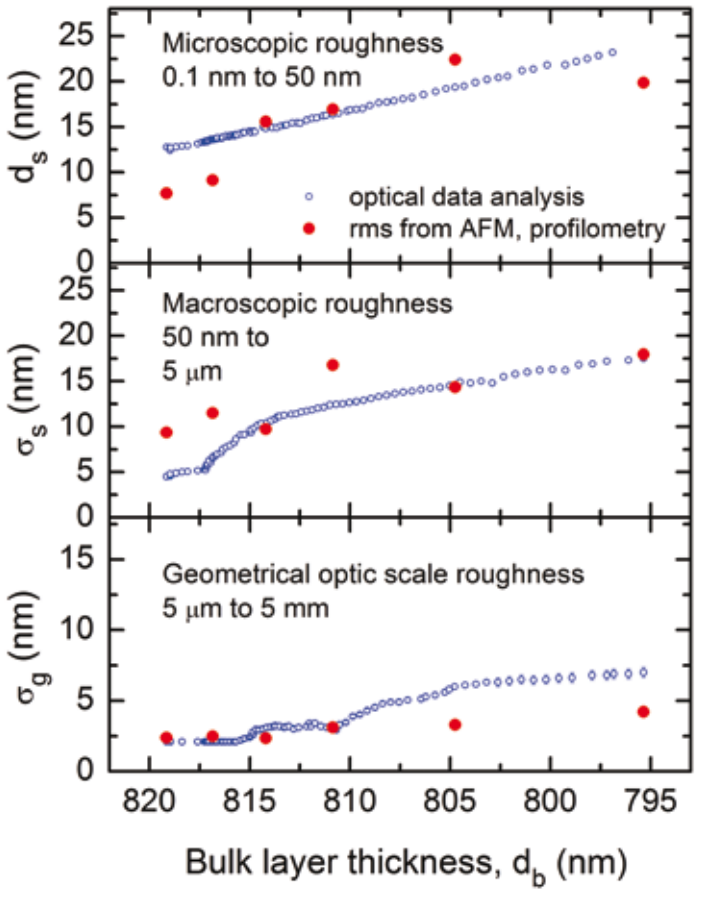

Figure 5. Evolution of surface roughness thicknesses on three different in-plane scales relative to the central wavelength λ ≈ 5000Å, obtained from a polarimetric analysis of spectra collected during ZnO:Al etching. These scales include microscopic (top, in-plane scale L << λ), macroscopic (centre, L ≈ λ) and geometric optic (bottom, L >> λ). The solid points are rms values of surface roughness from atomic force microscopy (AFM) (top: from 0.2 × 0.2μm^2 images, and centre: from 10 × 10μm^2 images) and profilometry (bottom: from 5mm-long traces).

Thin-film Si:H photovoltaics

Optical properties

The optical properties of amorphous semiconductor alloy thin films, including hydrogenated amorphous silicon (a Si:H), amorphous silicon-germanium (a-$Si_{1-x}Ge_x$:H), and amorphous silicon-carbon (a-$Si_{1-x}C_x$:H), incorporated as the *i*-layers in solar cells, have been determined in situ in the research laboratory using real-time SE. These optical properties can be expressed in terms of a relatively small number of wavelength-independent parameters [3]. In fact, for a set of alloys of highest PV quality at any given temperature of measurement, the optical properties can be determined through specification of a single parameter – the optical bandgap value. This is possible via a Kramers-Kronig consistent mathematical expression in which each parameter is linked to the bandgap. Fig. 6 shows these sets of optical properties, generated mathematically for three different bandgap values E_g. The optical properties of each set are given in the forms (ε_1, ε_2) and (n, α), where $\varepsilon_1 = n^2 - k^2$ and $\varepsilon_2 = 2nk = n\lambda\alpha/2\pi$. In modelling other amorphous PV materials such as doped layers, or *i*-layers prepared

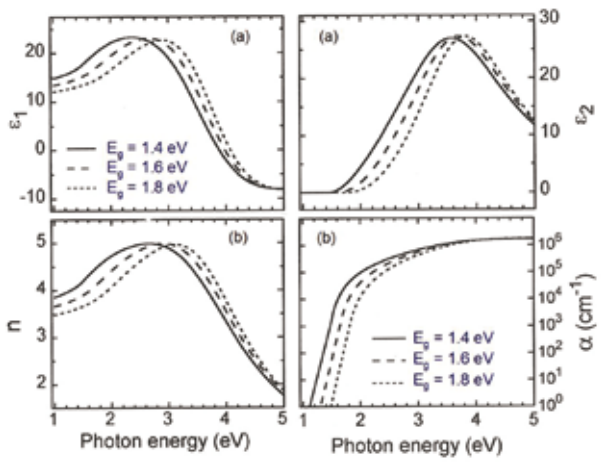

Figure 6. Room temperature optical properties (a) (ε_1, ε_2) and (b) (n, α) for hypothetical hydrogenated amorphous silicon (a-Si:H) alloys of optimum PV quality, computed on the basis of a single specification of the optical bandgap E_g. These results were deduced from an analytical expression that includes 1) Lorentz oscillator behaviour at high energies, 2) a bandgap onset consistent with parabolic densities of states and a constant dipole matrix element, and 3) an exponential Urbach tail connecting to the absorption onset at low energies.

differently from the standard optimized radio-frequency (RF) plasma-enhanced chemical vapour deposition (PECVD) method, then additional parameters must be incorporated in order to decouple the energy, width and amplitude of the oscillator feature in Fig. 6 from the bandgap. These additional parameters may include the void volume fraction and the Lorentzian oscillator width.

On-line roll-to-roll monitoring

Fabrication of thin-film a-Si:H *n i-p* solar cell stacks has been investigated using PECVD within a cluster tool having roll-to-roll cassette capability [9]. The substrate for the solar cell stack is flexible plastic in the roll-to-roll configuration, coated with a back reflector (BR). Real-time monitoring of the thin-film deposition processes has been performed by SE at an incidence angle of 65 degrees, using a rotating compensator multichannel instrument with a spectral range of 0.75–5.8eV (M2000-XI, J.A. Woollam Co.) [5–7]. Monitoring occurs at the centre line of the 15cm-wide substrate at a fixed point within the 18cm-long PECVD zone, located 13cm from the entry point of the substrate as shown in Fig. 7. The emphasis of this discussion is the topmost Si:H *p*-layer, because of the need to carefully control its thickness (at ~100Å), optical properties and phase in the solar cell in order to optimize the open-circuit voltage and blue response. The goal of this investigation is to monitor the growth of the *p*-layer at high hydrogen dilution ratio R (R = [H_2]/[SiH_4]) versus thickness after plasma ignition over the leading end of the substrate roll, in a test-run as the layer progresses through the a-Si:H (or so-called 'protocrystalline' Si:H), mixed-phase amorphous+nanocrystalline (a+nc)-Si:H and single-phase nanocrystalline (nc)-Si:H growth regimes.

After *p*-layer deposition, the leading end of the roll has been measured across its full width using ex situ mapping SE (AccuMap-SE, J.A. Woollam Co.) over the range of 0.75 to 6.5eV, with a 1 × 1cm^2 grid in order to characterize the *p*-layer uniformity before deposition of the final indium-tin oxide top contact. From the leading end of the roll, the *p*-layer exhibits an approximately linear thickness gradient over the start-up length (i.e. the length of the PECVD zone), because increasing distances along the substrate from this end have spent an increasing amount of time within this zone. Thus, using ex situ mapping SE, the spatial phase diagram of the *p*-layer

can be identified across the 15cm width and 18cm start-up length of the roll. Such a spatial phase diagram identifies the regions of the roll where protocrystalline Si:H, mixed-phase (a+nc)-Si:H and single-phase nc-Si:H appear at the near surface of the *p*-layer. The phase diagram allows one to develop the deposition process and substrate speed to ensure a uniform high-quality protocrystalline Si:H *p*-layer over the entire area of the flexible substrate, as desired for optimization of *n-i-p* solar cell performance in the substrate/BR/*n-i-p* configuration [15].

To achieve this level of understanding of the deposition process, the *p*-layer was deposited on Cr/Ag/ZnO/*n*/*i*-layer at a slow web speed and monitored by real-time SE. A slow speed is used such that the *p*-layer initially evolves through the desired protocrystalline phase, but then transitions first to mixed-phase, and finally to single-phase nc-Si:H in the time that it takes the web to cross the full deposition zone. In contrast, an optimized process requires a higher web speed, ensuring that the maximum *R* value is used while avoiding nanocrystallite nucleation for an ~100Å *p*-layer [15]. In fact, after the initial leading end is coated at the slow web speed for *p*-layer analysis purposes, the web can be accelerated to a higher speed and the *R* value can be adjusted as needed to achieve their optimum values. The phase diagram for a slow web speed is identified through the roughness evolution from the real-time SE analysis, which can be confirmed in a subsequent comparison with the mapping results obtained along the centre line of the substrate roll.

For the fabrication of an *n-i-p* solar cell, several deposition steps were performed before the critical *p*-layer. First, the polyethylene naphthalate (PEN) plastic was fully coated with Cr metal, which acts as an adhesion layer. On top of the Cr, an opaque Ag metal film was sputter deposited, followed by a 3000Å ZnO:Al layer to form the back reflector. Next, a 200Å-thick a-Si:H *n*-layer and a 3000Å-thick *i*-layer were deposited by PECVD. As the last silicon PECVD step, which was the focus of this study, the thin *p*-layer was deposited at a substrate temperature of 110°C, with an RF power of 40W, a pressure of 1.5Torr, and flows of 2sccm SiH_4, 300sccm H_2 (resulting in R = 150) and 0.5sccm dopant gas (5% B_2H_6 in H_2; resulting in D = $[B_2H_6]/[SiH_4]$ = 0.0125). Both the pressure and the RF power were fixed, starting from plasma ignition and continuing throughout p-layer growth. At the slow web speed of 0.015cm/s, the effective *p*-layer thickness reaches ~800Å after the web traverses the full 18cm deposition zone, as determined by the mapping SE measurement. The real-time SE measurement can observe at most only a fraction of ~0.7 (13cm/18cm)

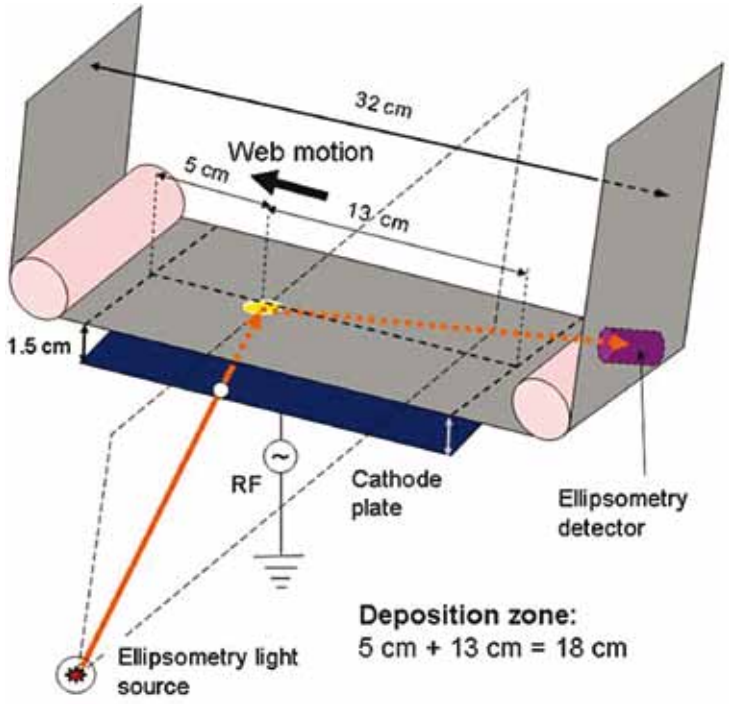

Figure 7. Schematic of the monitoring configuration used for real-time spectroscopic ellipsometry (SE) of a-Si:H *n-i-p* solar cells fabricated by plasma-enhanced chemical vapour deposition (PECVD) in a cassette roll-to-roll cluster tool. For deposition of the *p*-layer, the plasma is ignited (at t_0) while the substrate is moving at a constant rate v. Under ideal growth conditions, the thickness at the monitoring point increases linearly from 0 at the rate $d(t) = (R_o/v)x(t)$; $0 \le x(t) \le x_0$, where R_o is the deposition rate and $x(t)$ is the distance of a point fixed on the substrate, as measured from the edge of the plasma zone at time t, defined so that $x(t_0) = 0$. Under ideal conditions, after a time $t = x_0/v$, the thickness saturates at $d = R_o x_0/v$, where x_0 = 13cm, the distance between the monitoring point and the edge of the plasma zone where the substrate first enters.

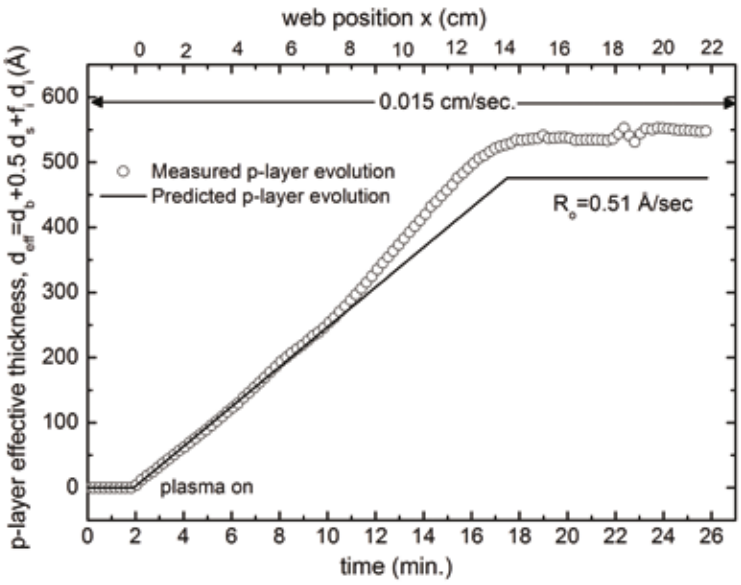

Figure 8. Evolution of the effective thickness as measured by SE during roll-to-roll deposition of a thin hydrogenated silicon (Si:H) *p*-layer at a web speed of v = 0.015cm/s on an underlying a-Si:H i-layer; also shown is a prediction (solid line) assuming a time- and position-independent deposition rate R_o within the plasma zone. The assumed rate of R_o = 0.51Å/s is that associated with an amorphous phase as measured in the early stages of growth.

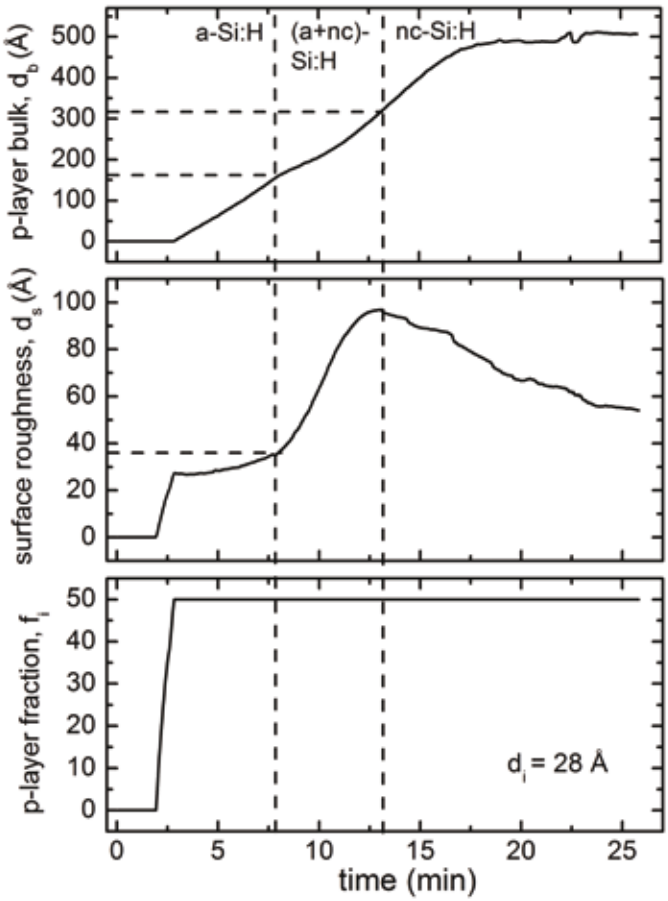

Figure 9. Evolution of bulk layer thickness (top), surface roughness layer thickness (centre) and interface filling fraction (bottom) during roll-to-roll PECVD of a thin-film Si:H p-layer at v = 0.015cm/s web speed on an underlying a-Si:H i-layer. In the bottom panel, a transition from *i*-layer surface roughness to *i*/*p* interface roughness occurs when the *p*-layer filling fraction reaches 50 vol%.

of this effective thickness development, or ~580Å, the deficit from 800Å being due to the deposition that occurs over the 5cm length beyond the monitoring point.

The optical properties of the underlying layers are needed to analyze the structural evolution of the *p*-layer and are obtained from analyses of data collected after depositing each layer in succession. The techniques used leading to these results are reported elsewhere in the paper. The opaque Ag and the ZnO:Al optical properties are generated by least-squares regression analysis [8], using a parameterization that includes a Drude component in the low-energy, near-infrared region and one or more critical point oscillator components in the high-energy, ultraviolet region [3]. The amorphous *n*, *i* and *p*-layer optical properties are generated using the same approach, but with the type of parameterization shown in Fig. 6. Fig. 8 shows the evolution of the *p*-layer effective thickness, which consists of interface, bulk and surface roughness thickness components, respectively, according to the expression $d_{eff} = 0.5d_i + d_b + 0.5d_s$. Also shown is a prediction (solid line) based on the assumptions of a constant deposition rate over time, starting from plasma ignition, and also uniformity of that rate along the centre line in the first 13cm of the deposition zone. Significant deviations from the prediction can be understood by considering the time evolution of the three individual components as shown in Fig. 9.

Before *p*-layer deposition, a microscopic roughness layer exists on the *i*-layer surface, as a 50/50 vol% mixture of *i*-layer/void. At the onset of deposition, the void component is filled in by the *p*-layer material in a time of ~1 minute, as shown in the bottom panel in Fig. 9 [16]. After 1 minute, the onset of bulk *p*-layer growth is observed on the resulting i/*p* interface roughness layer (top panel in Fig. 9). The surface roughness and bulk layer thickness evolution for the *p*-layer suggests that the *p*-layer grows initially in the amorphous phase. The layer undergoes an amorphous to mixed-phase (a+nc) transition at ~8 minutes, occurring after ~155Å of bulk *p*-layer deposition and at which point the surface roughness shows an abrupt increase. Thus, the acceleration of the *p*-layer deposition rate in Fig. 8 starting from ~8 minutes can be attributed to a higher growth rate for the nc-Si:H phase compared with the protocrystalline Si:H phase [17].

After the mixed-phase growth regime, the *p*-layer undergoes a mixed- to single-phase nc-Si:H transition at ~13 minutes when the surface roughness reaches its maximum and begins to decrease. This transition occurs after ~320Å bulk *p*-layer thickness. The decrease in surface roughness is attributed to the coalescence of inverted conical crystallites that protrude above the surface; the result is single-phase nc-Si:H [17]. The thickness saturates at 17 minutes, at which time the moving web has fully crossed the deposition zone. For later times, all film characteristics should stabilize at the values obtained at 17 minutes; however, the continued decrease in roughness suggests a temporal non-uniformity such that crystallite nucleation and coalescence is favoured with increasing duration after the plasma ignition.

> "Optimizing the deposition process and ensuring that the web is uniformly flat by maintaining constant tension across the width can improve the p-layer thickness uniformity at the desired final thickness."

The ex situ mapping result of the *p*-layer deposited at 0.015cm/s is shown in Fig. 10. Here, the surface roughness evolution (Fig. 10(a)) along the central line is in good agreement with that of the real-time SE result. The mapping result also demonstrates that the *p*-layer film initially grows in the a-Si:H (or protocrystalline) phase, transitions to mixed-phase (a+nc), and finally coalesces into single-phase nc-Si:H. The mixed-phase transition occurs when the surface roughness layer is ~30Å; above that thickness, there is a sharp increase in the roughness thickness as indicated in the real-time SE result of Fig. 9 (centre panel). Thus, the amorphous- to mixed-phase transition line is drawn on the surface roughness thickness map where this abrupt increase is observed (left broken line). By superimposing this transition line onto the bulk layer thickness map (Fig. 10(b)), the amorphous- to mixed-phase transition is observed to occur at bulk layer thicknesses from 30 to 200Å, depending on the substrate location. Similarly, the transition from the mixed-phase (a+nc) to single-phase nc-Si:H occurs where the surface roughness thickness reaches a maximum (right broken line). By superimposing this transition line onto the bulk layer thickness map, the transition is

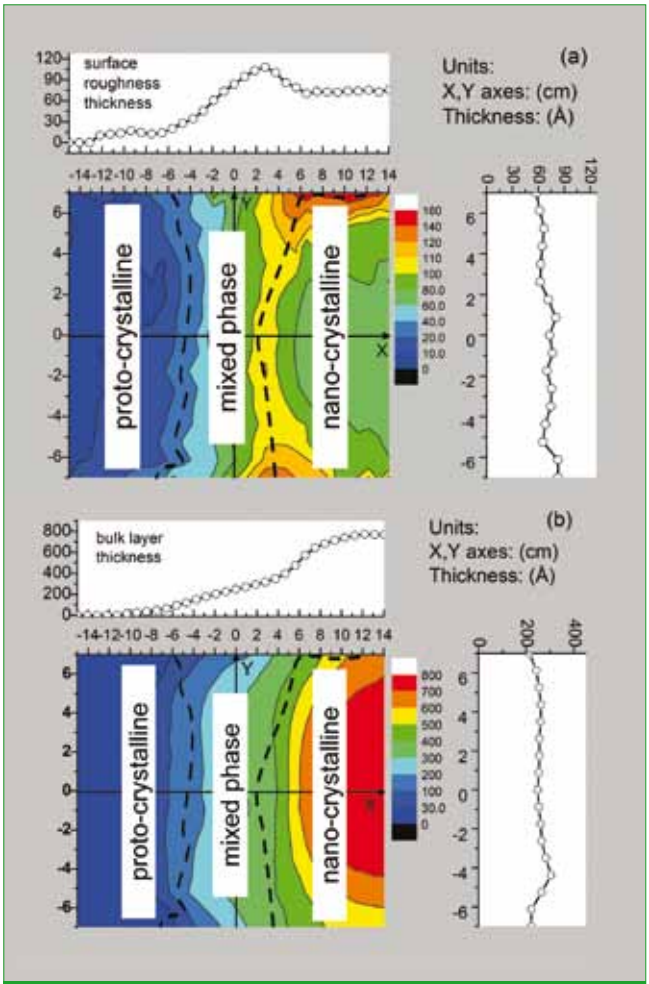

Figure 10. Maps of (a) *p*-layer surface roughness and (b) *p*-layer bulk thicknesses deposited at a web speed of *v* = 0.015cm/s on PEN polymer coated with a Cr/Ag/ZnO/*n*/*i* layer. The broken line on the left indicates the locations at which the amorphous to mixed-phase amorphous+nanocrystalline (a+nc) Si:H transition occurs at the top of the deposited *p*-layer. The broken line on the right indicates the locations at which the mixed-phase to single-phase nanocrystalline (nc) Si:H transition occurs at the top of the *p*-layer.

observed to occur at bulk layer thicknesses over the range of 300 to 600Å. The lines on the bulk layer thickness map establish the spatially dependent phase diagram for $R = 150$.

The thickness maps enable one to evaluate the uniformity along the width of the flexible substrate. From Fig. 10(b), it is clear that the bulk *p*-layer thickness is greater in the central region than at the edges. The effect is enhanced in the nc-Si:H growth regime, possibly due to the higher growth rate of the nc-Si:H phase, coupled with the apparent lower nanocrystal nucleation density near the edges, as noted below. A thicker layer at the centre may also occur if the plastic is slightly warped so that the central portion of the plastic is closer to the cathode plate than the edges. Below the transition to single-phase nc-Si:H, the surface roughness layer tends to be larger near the centre of the substrate; however, near and above this transition, the situation is reversed. The net effect of the observed behaviour is that, near the edge of the substrate, nucleation occurs at a lower thickness and the density of these nuclei appears to be lower since the coalescence occurs at a somewhat greater bulk layer thickness [17]. Since the web speed determines the time during which the substrate resides in the deposition zone, the desired final thickness can be obtained by choosing the web speed proportionately. Optimizing the deposition process and ensuring that the web is uniformly flat by maintaining constant tension across the width can improve the *p*-layer thickness uniformity at the desired final thickness.

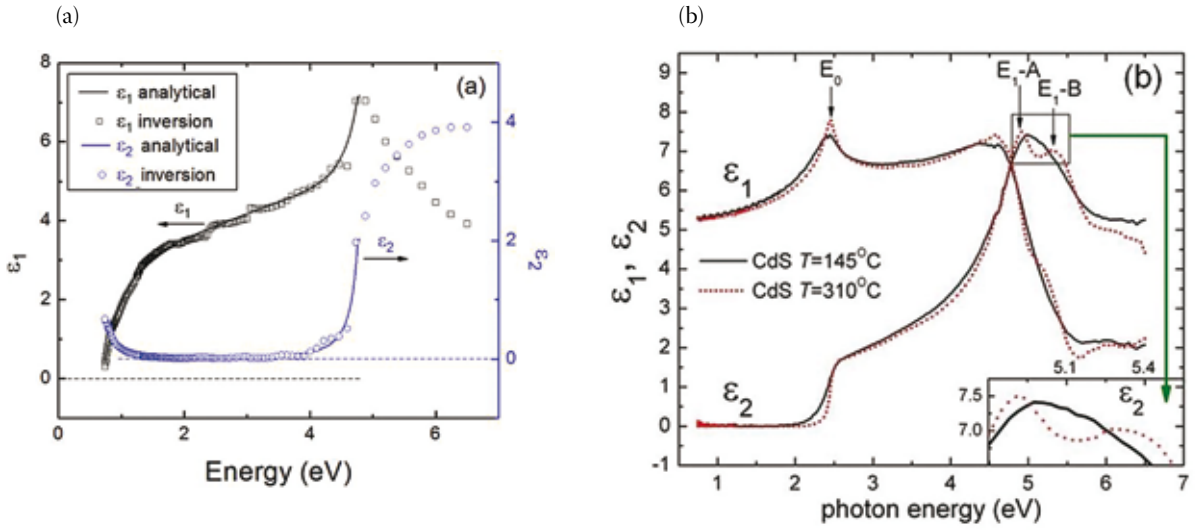

Figure 11. (a) Room temperature dielectric function of the topmost SnO_2:F layer of NSG-Pilkington TEC-15 glass; both methodologies of exact inversion (points) and analytical fitting below 4.8eV (lines) are shown and are in good agreement; (b) room temperature dielectric functions of two cadmium sulphide (CdS) thin films prepared by magnetron sputtering at substrate temperatures of 145°C and 310°C.

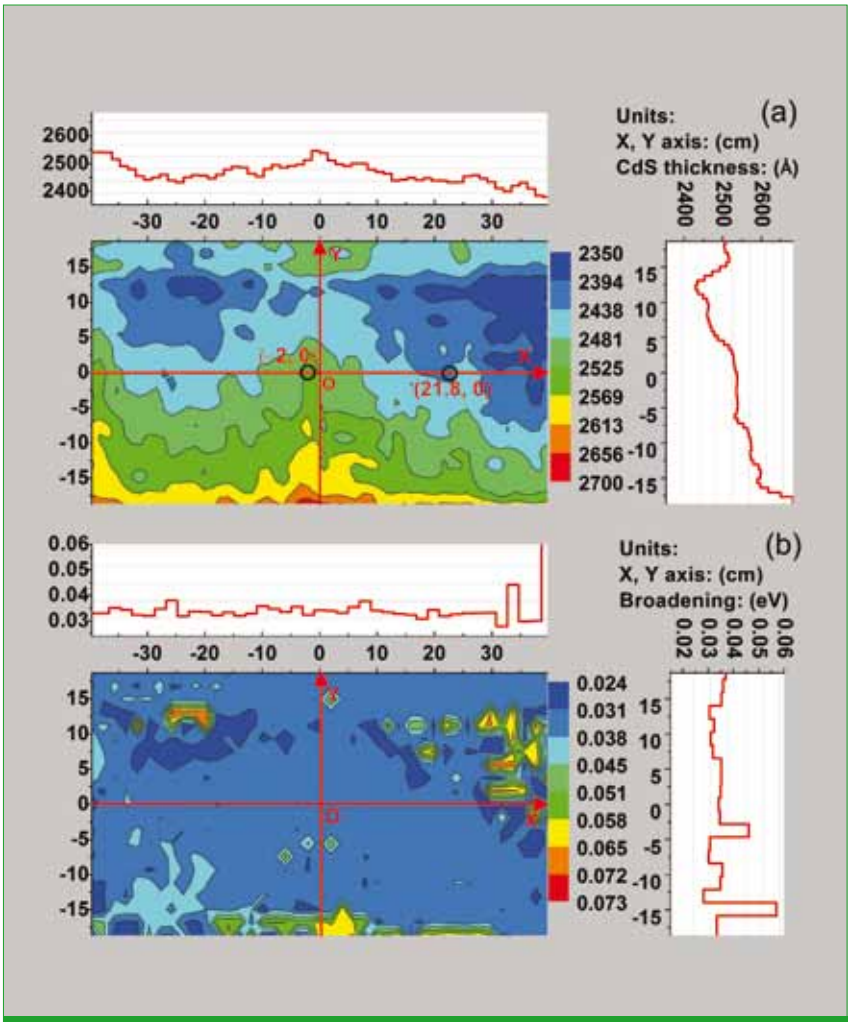

Figure 12. Maps of (a) CdS bulk layer thickness and (b) E_0 critical point (CP) broadening parameter over an ~40 × 80cm² region of a PV plate consisting of coated glass. The CdS film was deposited by atmospheric pressure vapour deposition on NSG-Pilkington TEC-15 glass for demonstration purposes (hence the large thickness). The plots in (a) and (b) (above and to the right of the maps) show the parameter variations along the X and Y axes. The experimental spectra and best-fit results for the two indicated points in (a) are given in Fig. 13.

CdTe photovoltaics

Optical properties

Application of SE and polarimetry methods for the characterization of the optical structure of CdTe-based thin-film PV requires a database of optical properties [18]. The semiconductor layers of the solar cell are deposited on soda-lime glass substrates coated with transparent conducting oxide (TCO). PV modules typically incorporate 60 × 120cm² glass panels and operate in the superstrate configuration, meaning that the solar irradiance passes through the coated glass on which the semiconductor layers are deposited. Standard coated glass (such as TEC-15 by NSG-Pilkington) consists of thin layers (~300Å) of undoped SnO_2 and SiO_2, and a thicker layer (~3000Å) of doped SnO_2:F.

The complex dielectric function spectra ε of the thicker SnO_2:F is the most critical among those associated with the TCO multilayer stack, and must be obtained in the completed stack using the ε spectra of the three underlying materials (glass, SnO_2, SiO_2) and the thicknesses of the thin SnO_2 and SiO_2 layers. To obtain the SnO_2:F dielectric function, a procedure was used that first applied mathematical inversion to the (ψ, Δ) spectra. To perform the inversion, the real and imaginary parts, ε_1 and ε_2, of ε were extracted in the analysis procedure simultaneously with the bulk and surface roughness layer thicknesses. The latter were selected by trial and error in an attempt to eliminate interference-related artefacts in ε_1 and ε_2 that appear in the semitransparent regime of photon energy (i.e. < 4.8eV) when the thicknesses are incorrectly selected [19]. Once the best results are obtained,

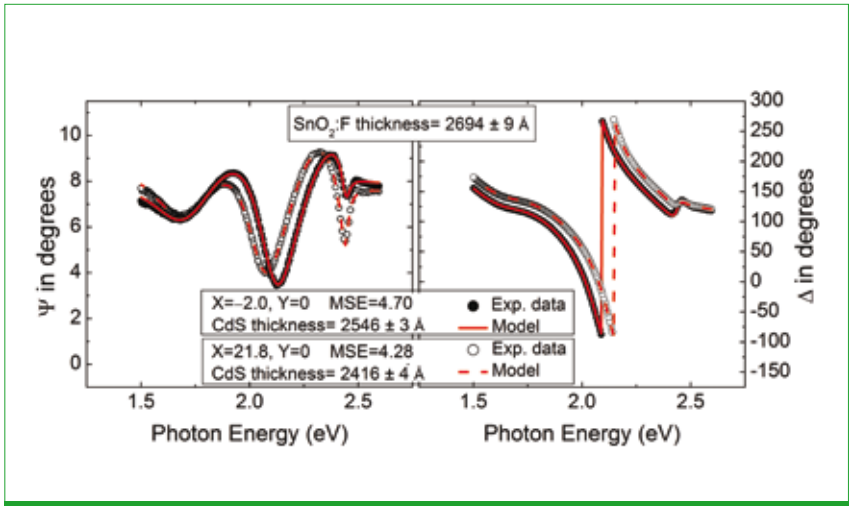

Figure 13. Experimental (points) and best-fit (lines) (ψ, Δ) spectra at positions (X = −2.0, Y = 0) and (X = 21.8, Y = 0) in Fig. 12(a), showing the effect of the CdS thickness on the data and fits. The SnO_2:F thickness was almost the same for the two positions and within 2694 ± 9Å. Confidence limits and mean square errors (MSEs) for the two best fits are also given.

an analytical model can then be used to smooth the inverted dielectric function and eliminate any residual artefacts that generally occur due to inadequacies in the optical model of the sample.

Fig. 11(a) shows the comparison of the inversion results for the topmost TEC-15 layer with the best-fit analytical expression below 4.8eV. Good agreement provides support for the overall analysis procedure. Above 4.8eV the inversion results were artefact free, so an analytical model was not needed. The analytical expression used a Drude free electron component due to free carriers in the SnO_2:F [20], a Sellmeier component to model the normal dispersive behaviour in ε_1, and a Lorentz oscillator to model the high energy absorption onset as evidenced by the increase in ε_2 above 4eV [3]. The Drude expression is given by:

$$\varepsilon(\omega)=\varepsilon_{0s}-\frac{N_{ec}e^2/\varepsilon_0 m_0}{\omega[\omega+i(2\Gamma_m/\hbar)]} \quad (1)$$

where ω is the optical frequency, ε_{0s} is a constant contribution ($\varepsilon_{0s}\geq 1$), N_{ec} is the free electron concentration, e is the electron charge, ε_0 is the free space permittivity, m_0 is the optical effective mass and ħ is Planck's constant. The Drude amplitude A and broadening energy Γ_m are given by $A^2 = N_{ec}e^2\hbar^2/m_0\varepsilon_0$ and $2\Gamma_m = \hbar/\tau$, respectively, where τ is the free electron relaxation time. These relationships can be used to deduce the electrical properties of the film, such as the optically extrapolated DC resistivity ($\rho = 2\hbar\Gamma_m/A^2\varepsilon_0$). From the thickness d of the SnO_2:F, the optically extrapolated DC sheet resistance is given by $R_s = \rho/d$.

It is also critical to parameterize ε of the cadmium sulphide (CdS) and CdTe layers that form the solar cell [18]. In this case, high-accuracy complex dielectric functions are obtained from films that are free of oxide overlayers via in situ measurements of thin films, followed by cooling and measurement at room temperature. Thicknesses in the 500–1000Å range are used for greater uniformity versus depth into the film. By monitoring the deposition by real-time SE during film growth, accurate bulk and surface roughness layer thicknesses are also obtained; these are not expected to change upon cooling to room temperature. Inversion in order to extract (ε_1, ε_2) of the thin film uses these accurate layer thicknesses.

As an example, the focus will be on the CdS layer, which is analogous to the top *p*-layer in the *a*-Si:H device to the extent that it serves as a window layer, and its optical properties and thickness have a significant effect on the blue response and thus short-circuit current of the solar cell. Fig. 11(b) shows the complex dielectric functions obtained in situ at room temperature for 500Å-thick CdS films prepared by magnetron sputtering at substrate temperatures of 145°C and 310°C with a fixed Ar pressure and flow of 10mTorr and 23sccm, and an RF target power of 50W [18]. The complex dielectric function spectra can be parameterized using an expression of the form as shown in Equation 2 [3], where the sum is over the three critical points (CPs), including the bandgap E_0, and E_1-A and E_1-B. The function f describes a broad background given as a Lorentz oscillator versus photon energy E with a well-defined energy onset E_g. For the nth critical point,

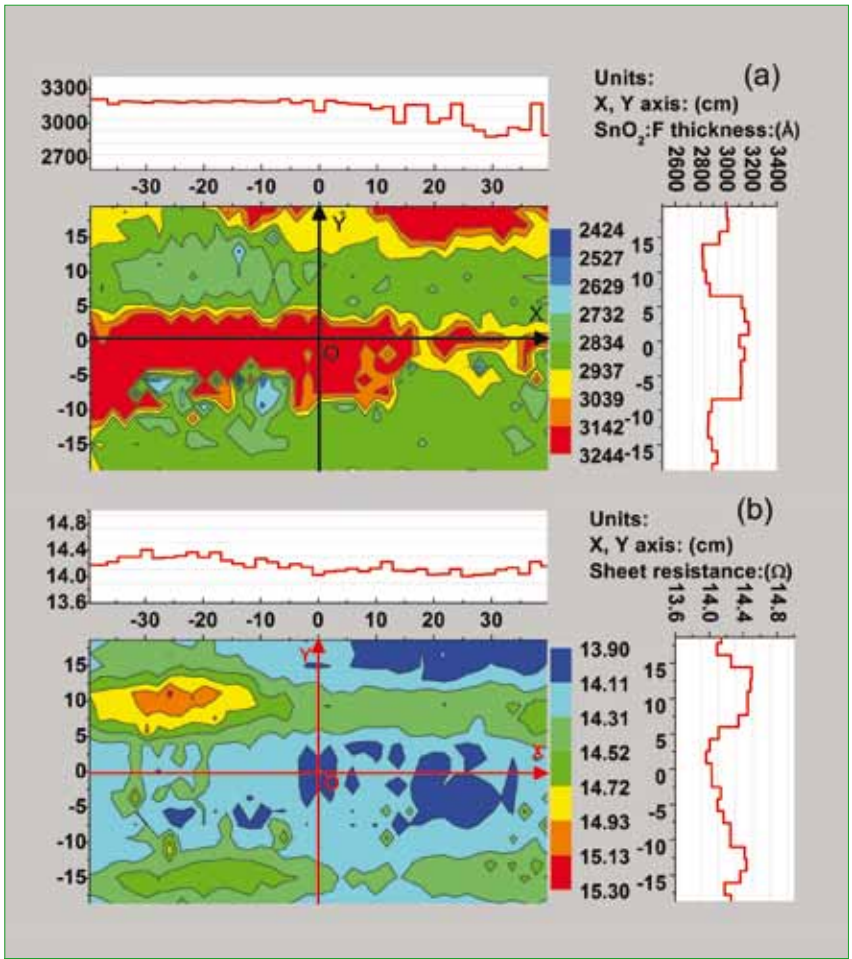

Figure 14. Maps of (a) SnO_2:F bulk layer thickness on the TEC-15 glass panel and (b) optical sheet resistance of the SnO_2:F layer. The plate in this case is the same as the one in Figs. 12 and 13; thus the SnO_2:F layer lies beneath the CdS layer. The plots in (a) and (b) (above and to the right of the maps) show the variations in the deduced parameters along the X and Y axes.

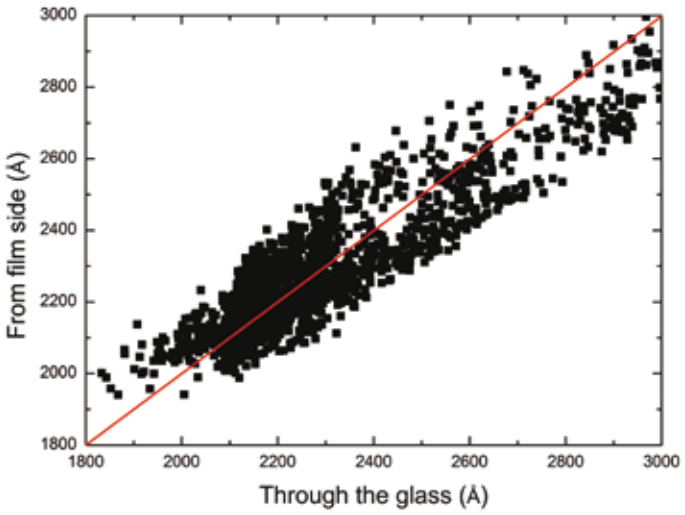

Figure 15. Correlation between the CdS thickness determined in a film-side measurement and the corresponding results obtained at the same position but through the glass. The scatter plot is obtained from individual measurements over the 40 × 80cm^2 region of the CdS-coated TEC-15 glass plate of Figs. 12–14.

A_n, E_n, Γ_n, μ_n and ϕ_n are the amplitude, energy, broadening parameter, exponent, and phase of the nth CP. For the Lorentz oscillator A_L, E_L and Γ_L are the amplitude, resonance energy and broadening parameter. In the parameterization of Equation (2), the exponents are fixed at the values obtained in the best fits to the single-crystal CdS complex dielectric function.

The most significant difference between the two spectra in Fig. 11(b) is in the widths Γ_n of the CP features, as shown in the inset for ε_2 of the two high-energy CPs labelled E_1-A and E_1-B. This difference can be attributed to variations in the average radius R of crystalline grains in the material. In addition, the CP energy positions can also vary due to stress in the films. Both effects can be quantified through the expressions:

$$\Gamma_n = \Gamma_{bn} + \hbar v_{gn}/R \quad (3a)$$

$$E_n = E_{bn} + C_{Xn} X \quad (3b)$$

where Γ_{bn} and E_{bn} are the broadening parameter and energy position for the single crystal in the limit of large R and zero stress. In Equation (3a), $\hbar$ is Planck's constant and v_{gn} is the group velocity associated with the nth CP; in Equation (3b), C_{Xn} is a stress coefficient. For a collection of samples fabricated under different conditions, the other parameters in Equation (2) can be either fixed or linked to the dominant parameters R and X. In this way, the number of variable parameters can be reduced from a total of 17 in Equation (2) to three which describe the physical properties of the sample, namely grain size R, stress X and void fraction f_v, the latter introduced independently through an effective medium theory.

Thus, the approach is similar to the one used to simplify the analysis of amorphous semiconductor films. The reason for this approach is clear. In fitting optical data for multilayer stacks, although all points in the 17-dimensional parameter space defined by Equation (2) are physically possible, only a small fraction of this space is accessible to CdS. By restricting the volume of accessible parameter space, the global minimum in the error function and the solution to the analysis problem can be located more easily and quickly. Furthermore, as a larger collection of materials with a wider range of properties is fabricated, the database can be modified to expand the parameter space and accommodate the new materials. As a result, optical property database development is a continuous 'work in progress.'

Off-line mapping

Off-line SE data have been collected from the film side over an ~40 × 80cm^2 area of a TEC-15 glass panel coated with CdS. These data have been analyzed using a five-layer model with free parameters that include the bulk and surface roughness layer thicknesses of the CdS and the three layer thicknesses of the TEC-15 glass substrate, including the SnO_2, SiO_2 and SnO_2:F [10]. The optical property parameters that are also incorporated in the modelling include the set of CdS CP broadening values which are linked to a single grain-size parameter R, and the Drude amplitude A and broadening Γ_m for the SnO_2:F layer that enables determination of the resistivity and sheet resistance of the layer.

Fig. 12 depicts maps of the CdS bulk layer thickness and the E_0 broadening parameter over the 40 × 80cm^2 area. The bulk layer thickness is observed to range from 2350 to 2700Å. These thickness values are much larger than those used in modules (typical values in modules are ~1000Å); thus, this plate is used for evaluating the SE mapping capabilities only. The effect of a 150Å difference in the CdS thickness appears clearly in the fringe patterns of the spectra in Fig. 13, and the difference is well described by the model. A larger broadening value in Fig. 12(b) is an indication of a smaller grain size R, or, more generally, a larger concentration of centres that scatter excited carriers. Smaller grain sizes in turn can result from a higher nucleation density in the deposition process. Regions with a larger E_0 broadening parameter in Fig. 12(b) appear to be correlated with reduced thickness or the presence of the plate edge.

Fig. 14 shows maps of the underlying SnO_2:F thickness and its sheet resistance, the latter obtained from the Drude parameters of the optical model as an extrapolation of optical frequency data. From the map in Fig. 14(a), the thickness of the topmost SnO_2:F layer of the TEC-15 stack is observed to vary between 2500 and 3250Å. In Fig. 14(b), only small variations in the optical sheet resistance are observed, ranging between ~14 and 15Ω/sq, with 15Ω/sq being the nominal value for TEC-15-coated glass panels.

The results in Figs. 12–14 are obtained from an analysis of SE data collected from the film side of the glass. This is preferable when the film stack is relatively thin (which generally implies that it is also relatively smooth) and when no single layer becomes optically opaque over a large part of the spectrum, which is the case for the plate studied here, consisting of glass/SnO_2/SiO_2/SnO_2:F/CdS. More often, however, in on-line applications it is more important to analyze the complete film stack, consisting of the TEC-15 glass and the CdS/CdTe heterojunction. Because the CdTe film used in PV modules is deposited to ~2–5μm, the resulting surface exhibits extensive microscopic, macroscopic and even geometric optics scale roughness, as well as being opaque at energies above 1.5eV, the CdTe bandgap. In this case, higher sensitivity to the underlying layers of CdS and SnO_2:F is obtained by directing the light beam through the glass.

In this optical configuration, various steps must be taken to optimize the measurement and analysis [21]. First, it is best to eliminate the ambient/glass reflection and measure

$$\varepsilon = \varepsilon_0 + \{\sum_{n=1}^{3} A_n[E - E_n - i(\Gamma_n/2)]^{\mu_n}\exp(i\phi_n)\} + f(E, A_L, E_L, \Gamma_L, E_g)$$

Equation 2.

only the glass/film-stack reflection; this is possible due to the relatively large thickness of the glass (~3.2mm) that leads to spatial separation of the two beams. Isolating the reflection from the glass/film-stack interface can be facilitated also by focusing the incident beam on that interface. Second, one must incorporate into the optical model a layer of different optical properties on the Sn bath side of the soda-lime glass, as well as stress in the glass. On its way from the source to the detector, the light beam makes two passes through the ambient/glass interface and through the glass itself, and the polarization modifications that occur in these passes differ from those predicted for a uniform slab of isotropic glass.

> "Among the features that may need to be incorporated for an improved correlation is an interface roughness layer between the SnO_2:F and the CdS, and an oxide-modified layer on the surface of the CdS."

In Fig. 15, the correlation between the CdS thickness as measured through the glass and from the film side is observed to be good; however, there is significant scatter. Among the features that may need to be incorporated for an improved correlation is an interface roughness layer between the SnO_2:F and the CdS, and an oxide-modified layer on the surface of the CdS. Thus, the optical model for the sample, and for PV multilayers in general, is a work in progress that must be improved over time along with the optical database.

Future directions in instrumentation for on-line SE

For the mapping ellipsometer used to obtain the results of Figs. 10 and 12–15, typical high-accuracy measurements are taken every ~5 seconds, including time for translating the ellipsometer, autofocusing and multiple optical cycle averaging. This relatively low measurement speed for mapping motivates future instrumentation development based on imaging [22–24]. A promising new approach developed by Fried and co-workers is to image the PV panel along a line across its width using an expanded light beam [11,23–24]. One dimension of a two-dimensional detector array is used for line imaging, and the second dimension is used for spectroscopic analysis. As a result, the data across the width of the panel are collected in parallel, significantly increasing the speed. Such instrument development is not without its challenges and, ultimately, limitations; however, the goal of future

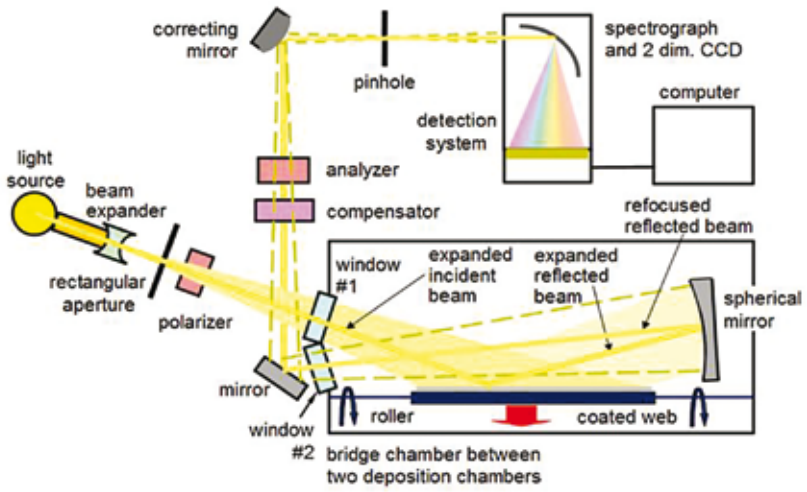

Figure 16. Simplified schematic of instrumentation for on-line SE imaging across the substrate width in conjunction with mapping along its length made possible by translation of the substrate on the production line. Although the design is shown for analysis of the coated substrate in roll-to-roll deposition, it can also be used in mapping moving glass panels.

efforts is to approach the high accuracy of the lower speed point-by-point approach in on-line applications.

Significant progress has been made starting from the original concept [11]. Characteristics of the instrument include an ~10-second measurement time for an image with 30 spatial points across the width of a 15cm wide panel, for a spatial resolution of ~0.5–1cm. Thus, in the current configuration, three to six line images can be generated at a substrate speed of 2–4cm/s. Two selectable spectral ranges from 350 to 650nm and from 650 to 1000nm have been used; the full range of 350 to 1000nm can be collected with a doubled line-image acquisition time of ~20 seconds. A total of 50 points are obtained over each range for a spectral resolution of 6–7nm. Consequently, each readout of the two-dimensional array leads to ~1500 spatial/spectral points. To reach the full potential of such an instrument, a 4× beam expansion to 60cm must be possible for on-line monitoring of CdTe PV panels, upscaling from the current width of 15cm, which is suitable for in situ analysis of roll-to-roll deposited materials as demonstrated in Figs. 7–10. Upscaling will require a brighter source and a more sensitive camera in order to maintain the current 0.5–1cm spatial resolution. Another expansion in instrument capability involves widening the spectral range with a single measurement cycle. This will require advanced polarizing optics (polarizers and compensators), along with multiple sources, and two-dimensional array detectors.

The current version of the line-imaging multichannel ellipsometer uses the rotating polarizer configuration of Fig. 1(a), in which case the rotations are performed step-wise rather than continuously [23,24]. In future developments of this expanded-beam imaging instrument, the step-wise rotating polarizer configuration should be replaced by the continuously rotating compensator, primarily to achieve improved performance for a wider variety of sample types, but also for a polarimetric capability critical for rough-surface applications.

An advantage of the point-by-point measurement approach is the ability to autofocus on the sample, maintaining a small spot size, and therefore to separate out the ambient/glass reflection in superstrate applications in which measurements are performed through the glass. In addition, an autoalignment capability enables determination of angle/plane of incidence corrections that are necessary for high accuracy when dealing with non-planar glass or flexible foil substrate surfaces. With the current expanded-beam instrument, line imaging is performed with a large depth-of-field pinhole camera, and angle of incidence and internal mirror calibrations are performed using planar wafer Si standard samples [24]. Advanced approaches must be developed for self-calibration as a component of data acquisition, which is possible to a limited extent with the rotating compensator configuration [25]. Corrections to calibration parameters may also be possible in data reduction, given sufficiently comprehensive models and optical property databases. The application of the imaging instrument for measurements through the glass is expected to be particularly challenging due to the incoherent superposition of ambient/glass and glass/film-stack interface images. With the depolarization information provided by the rotating

compensator configuration, it may be possible to address these challenges.

As shown by the simplified schematic of Fig. 16, the expanded-beam ellipsometer has a critical advantage in that the full width of the PV panel can be probed with a single beam that enters and exits through individual viewports. In fact, no moving optical components are needed. This approach enables in situ monitoring of PV panels under vacuum, in particular in roll-to-roll systems, utilizing bridge chambers between successive deposition chambers for the purposes of in situ monitoring of each critical thin-film fabrication step, before the next step is performed. This capability is expected to assist in optimizing and troubleshooting processes during equipment installation, enhancing yields during production and identifying equipment maintenance issues that require shutdown.

Summary

This paper has reviewed the current state of the art in polarization spectroscopy for in situ, real-time and off-line analysis of the uniformity of thin-film PV materials, including multilayers on rigid glass as well as on flexible metal and polymer foil substrates. The example given for in situ, real-time spectroscopy comes from process development and optimization of roll-to-roll fabrication for thin-film hydrogenated amorphous silicon (a-Si:H). In this example, the flexible substrate/film is probed at a single fixed point along the centre line of the substrate as it moves through the deposition zone. The critical topmost *p*-type layer of the *n-i-p* solar cell has been studied, since a very thin amorphous film having the more ordered protocrystalline structure is desired. The first large-area off-line mapping example is demonstrated in this *p*-layer study, in which the uniformity across the width of the substrate/film stack is evaluated. A second example is shown, in which the uniformity in the properties of a partially completed CdTe PV panel of CdS-coated glass is evaluated. The thickness and properties of the critical CdS layer have been obtained; a very thin polycrystalline film with low defect density is desired in this application. In general, a significant component of the methodology development effort occurs in the research laboratory through the construction and verification of optical models, in particular approaches for working with very rough surfaces; the accumulation of optical property databases; and the evaluation of new instrument design concepts.

The construction of optical models involves incorporating non-idealities such as graded optical properties in bulk layers, interdiffusion at interfaces and substrate-related artefacts (for example ambient/glass reflections) as well as the features of surface and interface roughness for a wide range of in-plane scales. Substrate-related artefacts become even more significant when measurements are performed through the glass. It is important to note that optical model development evolves over time, as previously unaccounted-for deviations between measured and best-fit ellipsometric spectra can be understood in terms of new optical features. There is also a close interrelationship between improvements in the optical model and improvements in the optical property database. The optical properties (n, k) of the materials that make up a thin-film PV stack can be parameterized using very general physics-based optical models; however, for polycrystalline semiconductors, the number of parameters in these expressions approaches 20 or more, depending on the number of band structure CPs in the studied spectral range. Optical property database development involves relating the optical property parameters to a much smaller number of parameters that describe basic physical properties of the materials. It is important to note that optical database development evolves as improved correlations between optical property parameters and basic materials properties are established.

This paper has demonstrated that useful information can be extracted in reflection from surfaces that exhibit roughness on a wide range of in-plane scales. Within scalar scattering theory, macroscopic roughness (having an in-plane scale of the order of the wavelength of the probe light) suppresses r_p and r_s equally, so its effect on (ψ, Δ) can be neglected. The resulting macroscopic roughness enables one to deduce a spectroscopic haze parameter for the film stack, which is inherently useful; however, the required irradiance calibration is challenging, especially in on-line environments. For geometric optics scale roughness, with an in-plane scale much larger than the wavelength, a key component of polarimetric analysis is the ability to separate out the depolarization that accompanies this roughness scale. An important future direction is to integrate and apply these capabilities in a wider variety of real-time applications, and in off-line and on-line mapping tools. Also, future research must be performed in the laboratory to evaluate the applicability of the scalar scattering theory under a wider range of conditions.

Future directions in adapting off-line mapping instrumentation to in situ and on-line applications have been identified. The off-line mapping examples demonstrated in this article employ relatively slow point-by-point measurement, in which the ellipsometer is translated over the surface of the sample. A solution to this problem, implemented by Fried and co-workers, is similar to that developed in transitioning to high-speed spectroscopy – namely, to incorporate parallel detection for the different spatial points across the width of the moving PV panel. As a result, the light beam is expanded to form a line over the width of the panel, and that line is imaged through a spectrograph onto one dimension of a two-dimensional array detector. The spectrograph disperses the image across the second dimension of the array for parallel spectroscopy performed simultaneously. Although challenges must be overcome to achieve the accuracy of the existing point-by-point mapping methods, the potential pay-off in terms of speed justifies further development of this approach.

References

[1] Ellison, T. et al. 2006, "Inline diagnostic systems for the characterization of multi-junction solar cells", *Proc. IEEE 4th World Conf. PVE Conv.*, p. 1736.

[2] Collins, R.W. et al. 2005, "Multichannel ellipsometry", in Tompkins, H.G. & Irene, E.A. (eds.), *Handbook of Ellipsometry*, William Andrew, Norwich, New York, p. 481.

[3] Collins, R.W. & Ferlauto, A.S. 2005, "Optical physics of materials", in Tompkins, H.G. & Irene, E.A. (eds.), *Handbook of Ellipsometry*, William Andrew, Norwich, New York, p. 93.

[4] Collins, R.W. et al. 2006, "The ultimate in real-time ellipsometry: Multichannel Mueller matrix spectroscopy", *Appl. Surf. Sci.*, Vol. 253, p. 38.

[5] Woollam, J.A. et al. 1999, "Overview of variable angle spectroscopic ellipsometry (VASE), Part I: Basic theory and typical applications", *SPIE Proc.*, Vol. CR-72, pp. 3–28.

[6] Johs, B. et al. 1999, "Overview of variable angle spectroscopic ellipsometry (VASE), Part II: Advanced applications", *SPIE Proc.*, Vol. CR-72, p. 29–58.

[7] Johs, B. et al. 2001, "Recent developments in spectroscopic ellipsometry for in situ applications", *SPIE Proc.*, Vol. 4449, pp. 41–57.

[8] Jellison, Jr., G.E. 2005, "Data analysis for spectroscopic ellipsometry", in Tompkins, H.G. & Irene, E.A. (eds.), *Handbook of Ellipsometry*, William Andrew, Norwich, New York, p. 237.

[9] Dahal, L.R. et al. 2010, "Application of real time spectroscopic ellipsometry for analysis of roll-to-roll fabrication of Si:H solar cells on polymer substrates", *Proc. 35th IEEE PVSC*, Honolulu, Hawaii, USA, p. 631.

[10] Huang, Z. et al. 2010, "Optical mapping of large area thin film solar cells", *Proc. 35th IEEE PVSC*, Honolulu, Hawaii, USA, p. 1679.

[11] Fried, M. et al. 2011, "Application of a dual-spectral-range, expanded-

beam spectroscopic ellipsometer for mapping large-area, laterally-inhomogeneous, photovoltaic multilayers", *Proc. Mater. Res. Soc. Symp.*, Vol. 1323, p. C3.12.
[12] Azzam, R.M.A. & Bashara, N.M. 1977, *Ellipsometry and Polarized Light*, North-Holland, Amsterdam.
[13] Fujiwara, H. et al. 2000, "Assessment of effective-medium theories in the analysis of nucleation and microscopic surface roughness evolution for semiconductor thin films", *Phys. Rev. B*, Vol. 61, p. 10832.
[14] Beckmann, P. & Spizzichino, A. 1963, *The Scattering of Electromagnetic Waves*, Pergamon, Oxford.
[15] Koval, R.J. et al. 2002, "Maximization of the open circuit voltage for hydrogenated amorphous silicon *n-i-p* solar cells by incorporation of protocrystalline silicon *p*-type layers", *Appl. Phys. Lett.*, Vol. 81, p. 1258.
[16] Koh, J. et al. 1995, "A real time spectroellipsometry study of hydrogenated amorphous silicon *p-i-n* solar cells: Characterization of microstructural evolution and optical gaps", *Appl. Phys. Lett.*, Vol. 67, p. 2669.
[17] Stoke, J.A. et al. 2008, "Optimization of Si:H multijunction *n-i-p* solar cells through the development of deposition phase diagrams", *Proc. 33rd IEEE PVSC*, San Diego, California, USA, pp. 413: 1–6.
[18] Li, J. et al. 2009, "Spectroscopic ellipsometry studies of thin film CdTe and CdS: From dielectric functions to solar cell structures", *Proc. 34th IEEE PVSC*, Philadelphia, Pennsylvania, USA, pp. 1783–1788.
[19] Aspnes, D.E., Studna, A.A. & Kinsbron, E. 1984, "Dielectric properties of heavily doped crystalline and amorphous silicon from 1.5 to 6.0 eV", *Phys. Rev. B*, Vol. 29, p. 768.
[20] Stjerna, B., Olsson, E. & Granqvist, C.G. 1994, "Optical and electrical properties of radio frequency sputtered tin oxide films doped with oxygen vacancies, F, Sb, or Mo", *J. Appl. Phys.*, Vol. 76, p. 3797.
[21] Chen, J. et al. 2009, "Through-the-glass spectroscopic ellipsometry of CdTe solar cells", *Proc. 34th IEEE PVSC*, Philadelphia, Pennsylvania, USA, p. 1748.
[22] Chegal, W. et al. 2004, "A new spectral imaging ellipsometer for measuring the thickness of patterned thin films", Jpn. *J. Appl. Phys.*, Vol. 43, p. 6475.
[23] Major, C. et al. 2008, "Wide angle beam ellipsometry for extremely large samples", *Phys. Stat. Sol.* (c), Vol. 5, p. 1077.
[24] Fried, M. et al. 2011, "Expanded beam (macro-imaging) ellipsometry", *Thin Solid Films*, Vol. 519, p. 2730.
[25] An, I. et al. 2004, "Calibration and data reduction for a uv-extended rotating-compensator multichannel ellipsometer", *Thin Solid Films*, Vols. 455–456, p. 132.

Acknowledgements

The authors would like to acknowledge the contributions of Chi Chen, Jie Chen, Andre Ferlauto, Zhiquan Huang, Christoph Ross, Carl Salupo and Christopher Wronski to this research and development. Support of this work was provided by the U.S. Department of Energy, Solar Energy Technologies Program, University Processes and Products Development Support Projects (Grant Nos. DE-FG36-08GO18073 and FG36-08GO18067), and by the State of Ohio Department of Development under the Wright Centers of Innovation Program.

About the Authors

Robert W. Collins is a distinguished university professor and NEG endowed chair in the Department of Physics and Astronomy at the University of Toledo, Ohio, USA. He co-directs the Center for Photovoltaics Innovation and Commercialization and has been involved in research and development of thin-film photovoltaics since 1976.

Lila Raj Dahal is a senior graduate student in the Department of Physics and Astronomy at the University of Toledo, Ohio, USA. He has been involved in research and development of thin-film Si:H photovoltaics since 2007. Lila has presented papers at several conferences in materials research and photovoltaics and authored a number of articles in conference proceedings.

Kenneth R. Kormanyos is the president and a senior research fellow of Calyxo USA. He is a co-inventor of the atmospheric pressure thin-film deposition technology employed by Calyxo GmbH for its manufacturing of CdTe photovoltaic modules. He has been involved with CdTe photovoltaics since 1998. Kenneth has nineteen US patents and six publications in the technical areas of PV manufacturing, tempering of low-ε glasses, natural gas-fired forced convection glass tempering systems, and compact systems for vitrification of hazardous or radioactive wastes.

Nikolas Podraza is an assistant professor in the Department of Physics and Astronomy at the University of Toledo, Ohio, USA. His research interests include optical characterization of materials, correlations between electrical and optical properties, and thin-film devices. Nikolas has authored more than 50 papers in peer-reviewed journals and conference proceedings.

Sylvain Marsillac is an associate professor in the Department of Electrical and Computer Engineering at Old Dominion University, Virginia, USA. He specializes in the science and engineering of the fabrication and characterization of solar cells. Sylvain has authored more than 100 papers in peer-reviewed journals and conference proceedings.

Enquiries

Center for Photovoltaics Innovation & Commercialization and Department of Physics & Astronomy
University of Toledo
Toledo, OH 43606
USA
Tel: +1 419 530 3843
Email: robert.collins@utoledo.edu

Calyxo USA
12900 Eckel Junction Road
Perrysburg, OH 43551
USA

Department of Electrical & Computer Engineering
Old Dominion University
Norfolk, VA 23529
USA